Local scrape-off layer control using biased electrodes in NSTX

S J Zweben, R J Maqueda[1]**, A L Roquemore, C E Bush**[2]**, R Kaita, R J Marsala, Y Raitses, R H Cohen**[3] **and D D Ryutov**[3]

Princeton Plasma Physics Laboratory, PO Box 451, Princeton, NJ 08540, USA
[1] Nova Photonics Inc., The Oak Place, Princeton, NJ 08540, USA
[2] Oak Ridge National Laboratory, PO Box 2008, Oak Ridge, TN 37831, USA
[3] Lawrence Livermore National Laboratory, 7000 East Avenue, Livermore, CA 94550, USA

Abstract
An experiment on the National Spherical Torus Experiment (NSTX) was designed to test the theory that biased electrodes can affect the local scrape-off layer (SOL) by creating a strong radial $E \times B$ flow (Cohen and Ryutov 1997 *Nucl. Fusion* **37** 621). These electrodes were located near the outer midplane and were biased at up to ± 90 V with respect to the local vacuum vessel ground. This biasing caused large changes in the local SOL profiles as measured by an array of Langmuir probes between the electrodes. A theory is presented which at least partially describes the experimental results.

(Some figures in this article are in colour only in the electronic version)

1. Introduction

It is well known that the highly localized power and particle flux to the divertor plates of a tokamak creates a difficult problem for the operation of ITER [1, 2]. This localization is due to the large ratio of parallel to perpendicular transport in the scrape-off layer (SOL), which causes the radial width of the SOL to be typically ~ 1 cm at the divertor plates. The radial transport depends upon both broadband turbulence and intermittent 'blobs' and cannot yet be predicted from first principles, so empirical scalings for the SOL width have been used to extrapolate to future devices, e.g. [3, 4].

Obviously it would be desirable to develop methods to externally control the SOL width of a tokamak. One proposal has been to apply toroidally asymmetric divertor plate biasing to create local convective cells to control the local radial SOL flow [5–7]. In this scheme the divertor plates would have isolated segments which are electrically biased with respect to each other to create a local poloidal electric field E_{pol}. Such a poloidal electric field in the presence of a magnetic field B could create a local radial plasma flow $v_{rad} = E_{pol} \times B$ flow which is larger than the radial flow speed of the turbulence, thus

leading to a radial displacement or broadening of the SOL at the divertor plate. Note that this type of biasing creates a toroidally *asymmetric poloidal* electric field, in contrast to many previous experiments which aimed to create a toroidally *symmetric radial* electric field [8, 9].

The present experiment was designed to test the basic principles of this theory using a small set of biased electrodes in the SOL near the outer midplane of NSTX. These electrodes had a strong local effect on the SOL profiles, but they did not (and were not designed to) affect the global plasma parameters. After a review of previous experiments in section 2, section 3 describes the experimental set-up in NSTX and section 4 describes the effects of biasing on the local SOL profiles. The effects of biasing on turbulence and other experimental results are in section 5, a comparison with the theoretical models is described in section 6 and a summary and discussion is in section 7.

2. Previous experiments

Most previous experiments on SOL biasing were designed to create a radial electric field in order to control the poloidal flow to improve the performance of poloidal divertors. A radial electric field was first used to modify plasma flow in the poloidal divertor of the Wisconsin Octopole [10], and several divertor plate biasing configurations were studied on the TdeV tokamak [11]. Control of particle exhaust was attempted using a biased toroidal divertor ring on DIII-D [12] and a biased pumped limiter in TEXTOR [13, 14]. Local radial electric fields were proposed to control the plasma interaction with RF antennas [15, 16]. There were also many experiments on plasma biasing inside the last closed flux surface to create a radial electric field in order to control edge transport, e.g. on TEXTOR [8, 9].

Other biasing experiments were done in the SOL of tokamaks to try to understand the perturbation along the magnetic field B due to Langmuir probes. A positive dc bias on a small plate in DITE changed the floating potential on a nearby probe ∼0.25 cm away along B, while a negative plate bias did not change the potential even at this small distance [17]. Probe biases were also detected very far along B; for example, both positive dc and 30 kHz oscillating probe bias in the SOL of TEXT were detected ∼12 m away along B [18], and a 60 kHz probe bias in the SOL of W7-AS was observed at a distance of up to ∼23 m away along B [19]. Changes in the local floating potential were also observed near biased divertor plate probes in Alcator C-Mod [20]. These issues concerning the parallel effects of biasing are important in the theory of Langmuir probes in a tokamak [21, 22].

Only a few previous experiments have attempted to measure convective cells and radial flows in the SOL generated using asymmetric biasing. In JFT-2M [23] an electrical bias of +120 V was applied to an inner wall divertor plate, and a poloidal electric field of ∼10 V cm^{-1} was measured at the midplane where the magnetic field lines connected to the biased plate. In MAST [24] an electrical bias of +80 to +120 V was applied to six toroidally separated divertor 'ribs', and the divertor strike point location (determined from the peak D_α emission) was shifted several centimeters radially outward in the expected $E \times B$ drift direction. In CASTOR [25] an electrode was biased +100 to +200 V in the SOL, a poloidal electric field of up to 5 kV m^{-1} was created on flux surfaces connected to the electrode and a strong poloidal modulation of the radial particle flux was measured. Therefore these experiments have demonstrated at least part of the physics described by the theory of asymmetric biasing [5–7].

Preliminary reports on the NSTX electrode biasing experiments described the diagnostics and electrode design [26] and the results from the first set of experiments [27]. This paper contains additional experimental results and more detailed analysis.
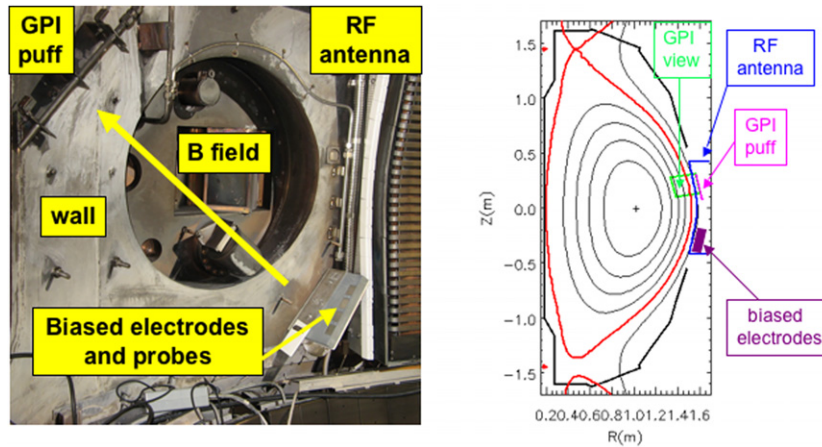
Figure 1. Photo of the outer wall of NSTX showing the location of the electrodes and probes in this experiment. The holder for the electrodes and probes was ∼25° below the outer midplane, and oriented so that the plane of the electrodes was approximately normal to the total magnetic field during plasmas. The electrode mounting plate was located ∼1 cm radially behind the shadow of the RF antenna just behind it. The gas puff imaging (GPI) manifold was ∼1 m along *B* in the other direction. The locations of the electrode holder and GPI diagnostic are also shown in poloidal cross-section.

3. Experimental set-up on NSTX

The general experimental set-up on NSTX is illustrated in figure 1. The electrodes are mounted into an insulating boron nitride holder located ∼25° poloidally below the outer midplane. Each electrode, as illustrated in figure 2, could be independently biased up to ±100 V with respect to the part of the stainless steel vacuum vessel wall located nearest the electrode holder. The electrodes were aligned approximately normal to the total magnetic field in this region. The leading edge of the mounting plate was ∼1 cm radially behind the leading edge of the nearby RF antenna limiter; thus the electrodes were in the SOL of this antenna and contacted the plasma in only one direction along *B* (the co-current and co-NBI direction). The field lines in this direction extended ∼1 to ∼8 m along *B* before hitting any other object in the SOL (depending on the details of the plasma equilibrium). The electrodes were at a fixed spatial location for these experiments.

A scale drawing of the electrodes is shown in figure 2, along with a schematic view of the applied poloidal electric fields and expected radial flows in this experiment. The four electrodes were 3 cm × 3 cm square stainless steel plates flush-mounted into the holder and separated in the local poloidal direction with a gap of 1 cm between them. The leading edges of the electrodes were 0.3 cm behind the leading edge of the holder. Each electrode could draw up to 30 A per electrode for positive bias or 10 A per electrode for negative bias. The electrode power supplies could be turned on versus off anytime during the discharge, and for the experiments described here were 100% modulated at 50 Hz for a clearer comparison of electrode on and off states. Each of the four electrode voltage and current signals were digitized at 20 kHz. All of the data in this paper were taken with biasing only on electrodes #2 and #3, with electrodes #1 and #4 grounded (unless otherwise noted).

The local effects of the electrode biasing were measured with a set of flush-mounted stainless steel Langmuir probes 0.3 cm in diameter, installed in the electrode holder as shown in figure 2. Five of these probes could be dc biased up to ±50 V with respect to the part of the
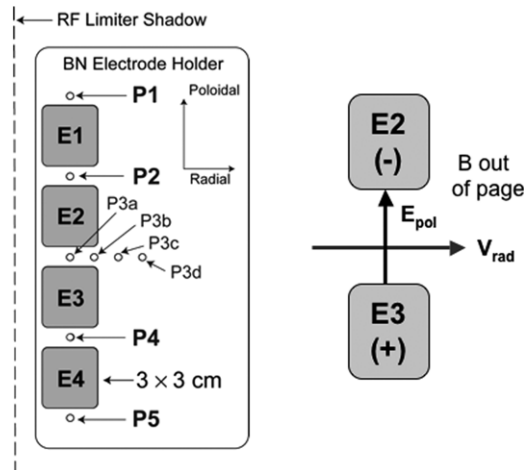
Figure 2. Scale drawing of the electrodes and probes along with a schematic view of the directions of the applied E_{pol} and expected V_{rad}. The four 3 cm × 3 cm electrodes were flush-mounted into a boron nitride holder and separated in the local poloidal direction with a gap of ∼1 cm between them. The leading edges of the electrodes were ∼0.3 cm behind the leading edge of the holder. There were eight flush-mounted stainless steel Langmuir probes with a 0.3 cm diameter in the electrode holder, four of them in a radial array between electrodes E2 and E3 (#P3a-P3d).

stainless steel vacuum vessel wall located nearest the electrode holder (see figure 1) or swept in voltage or 'floated'. Most of the results in this paper were taken using the four probes in the radial array P3a-P3d, which have a radial probe-to-probe separation of 1.25 cm. The current and voltage signals from the probes were digitized at 200 kHz. Both the electrodes and the probes had ∼1 mm gaps at and below their edges to prevent arcing, and no arc tracks between electrodes and/or probes were seen after the run.

The other main diagnostic used in this experiment was the gas puff imaging (GPI) system, also shown in figure 1. The GPI system measures the radial versus poloidal distribution of the D_α light emitted by a controlled D_2 gas puff in the edge and SOL. The measured D_α emission is a function of the local electron density and temperature, as well as the neutral density introduced by the gas puff. The GPI camera records the D_α images at a fast framing rate (∼10 μs/frame), so it can measure the effects of slow profile changes as well as fast turbulence. The GPI gas puff manifold was located ∼1 m along B from the biased electrodes. This was used to measure the effects of electrode biasing on the SOL plasma at this location, as described in section 5.2. Further information concerning the electrodes and probe hardware for this experiment are described elsewhere [26, 27], and information on the GPI diagnostic on NSTX can be found in [28].

4. Effects of biasing on the local radial profiles

This section describes effects of electrode biasing on the radial array of Langmuir probes between the biased electrodes E2 and E3, as shown in figure 2. These electrodes had a strong local effect on the SOL profiles near the electrodes, but were not designed to (and did not) affect the global plasma parameters.

The results of sections 4.1–4.3 are for Ohmic lower single null diverted deuterium plasmas with typically $R = 0.85$ m, $a = 0.65$ m, $B_o = 0.45$ T, $I = 0.8$ MA,
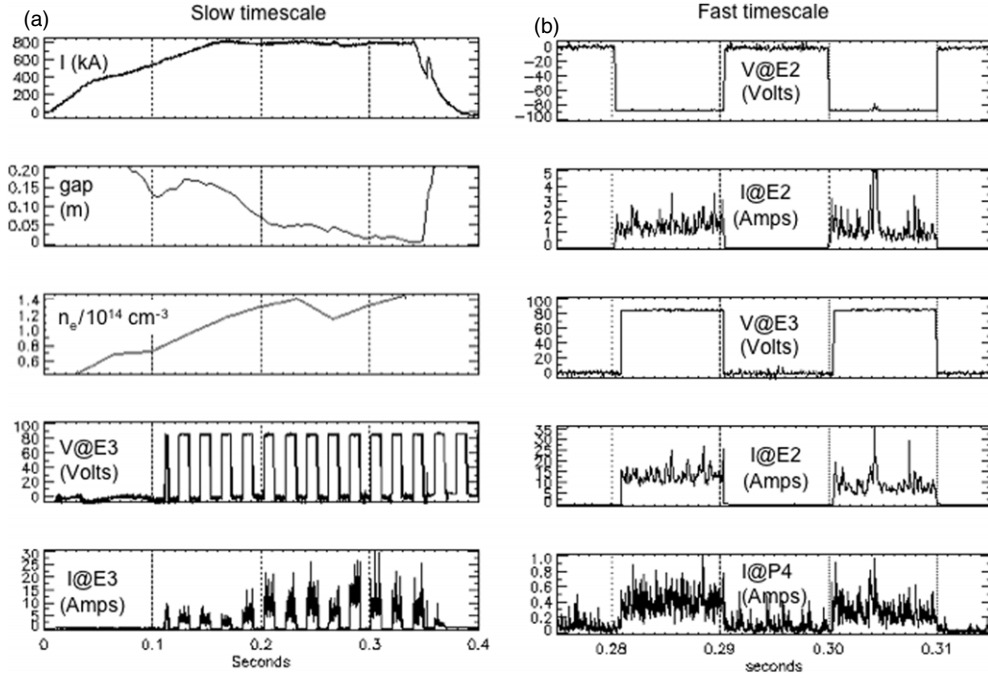
Figure 3. Typical time dependences of some plasma parameters along with electrode and probe signals (#129501). On the slower timescale in (*a*), the plasma current, outer gap, and line-averaged density are shown along with the electrode voltages, which were 100% modulated at 50 Hz (at constant voltage). On a faster timescale in (*b*) are the electrode voltages and currents, and also a probe current (bottom trace). The high frequency fluctuations in the electrode and probe currents are due to SOL turbulence.

$\langle n_e \rangle \sim (1.0\text{--}1.5) \times 10^{13}\,\text{cm}^{-3}$, $T_e(0) \sim 0.5\text{--}1\,\text{keV}$, κ (elongation) ~ 2, with a *B* field angle near the outer midplane of $\sim 40°$ from the horizontal (as is typical of spherical tokamaks), and $P_{OH} \sim 1\text{--}2\,\text{MW}$. The divertor X-point was formed before the current flat-top time at 0.2 s, the fueling was through gas puffing, and the carbon walls were conditioned with boron and lithium coatings. Section 4.4 describes the (qualitatively similar) results for NBI and RF heated plasma. For sections 4.1–4.4 the electrodes E2 and E3 were biased (−) and (+), respectively, with respect to the part of the vacuum vessel wall located nearest the electrode holder (see figures 1 and 2), such that their local poloidal electric field should produce a radially outward plasma flow. Section 4.5 describes results with several different electrode polarities.

4.1. Time dependences

A typical time dependence of the electrode voltages and currents in this experiment is shown in figure 3. Since the SOL density varied on a slow timescale with the normal evolution of the main plasma density, and also with the width of the 'gap' between the separatrix and the outer midplane limiter, the electrode bias voltages were all 100% modulated at 50 Hz to allow a nearly continuous comparison between the 'bias on' (with respect to the vessel ground) versus the 'bias off' (i.e. floating) states. There was also occasionally a transient variation in the electrode current (and corresponding SOL density) with strong MHD activity, as occurred at ∼0.25 s in this particular discharge. Therefore the data analysis for this experiment was averaged over many (∼10–30) bias on/off cycles over, and over several discharges, to minimize the effects
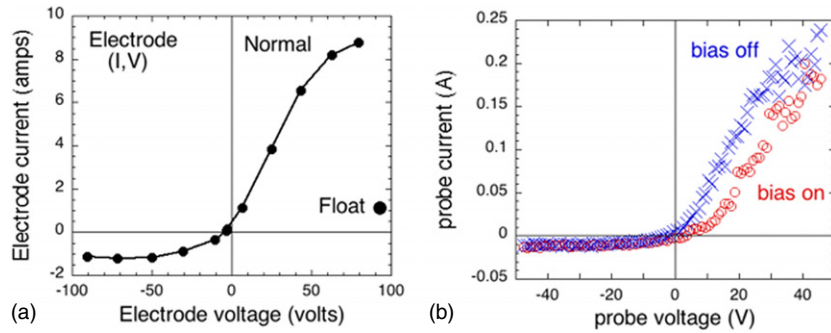
Figure 4. Electrode and probe (I, V) characteristics. Plot (a) shows the dependence of the electrode current with the electrode voltage. The 'normal' curve is for the usual case where the electrodes are biased with respect to the (grounded) wall. Each point represents the current drawn by either the positively biased electrode E3 or the negatively biased electrode E2, averaged over 0.2–0.3 s in similar shots. The 'float' point was when the electrode E3 was biased with respect to E2. Plot (b) shows the current versus voltage for probe #P3a, both with 'bias on' (E3 at +90 V and E2 at −90 V) and 'bias off'. The probe points are each averaged over all voltage sweeps in the steady-state part of the discharge (#129506).

of both these slow and transient variations. On a faster timescale, as shown on the right of figure 3, the electrode currents responded within 1 ms to changes in the electrode voltages, as did the signals from the probes. The large fast fluctuations on the electrode and probe currents are due to SOL turbulence.

4.2. Electrode and probe characteristics

Figure 4(a) shows a typical (I, V) characteristic for the electrodes in the voltage range −90 to +90 V with respect to the nearby vessel ground, i.e. 'normal' biasing. The positive bias values were for the bias applied to electrode E3 and the negative values for the bias applied to electrode E2 for a set of identical plasmas similar to that of figure 3 (#129500–129505), and the electrode voltage and current were time-averaged over all the 'bias on' periods from ∼0.2–0.3 s. The ratio of electrode electron current at +90 V to electrode ion current at −90 V was ∼8, and the floating potential of the electrodes was ∼0 V. Also shown in figure 4(a) is a 'floating' current point obtained on similar discharges when electrode E3 was biased at +90 V with respect to electrode E2, i.e. with both electrodes floating with respect to the vessel ground (see section 4.6).

Figure 4(b) shows a typical (I, V) characteristic for one of the probes, in this case probe P3a between electrodes E2 and E3. For this shot (#129506) the probe voltage was swept between ±50 V at 200 Hz, and curves for the electrodes 'bias on' (E2 = −90 V, E3 = +90 V) and 'bias off' are shown separately. These curves are each averaged over all the available voltage sweeps during the steady-state part of the discharge periods from ∼0.2–0.34 s, and the results are binned in 1 V increments. The electron current does not show a clear saturation, as usual for probes in a strongly magnetized plasma, and the ratio of the probe electron current at +45 V to the probe ion current at −45 V was ∼15–20. The ratio of the ion current in the electrode E2 at −90 V to the ion current in the nearby probe (P3a) at −50 V is ∼(1 A/0.01 A) ∼ 100, which is near to the ratio of the electrode area to the probe area (∼9 cm^2/0.07 cm^2), as expected.
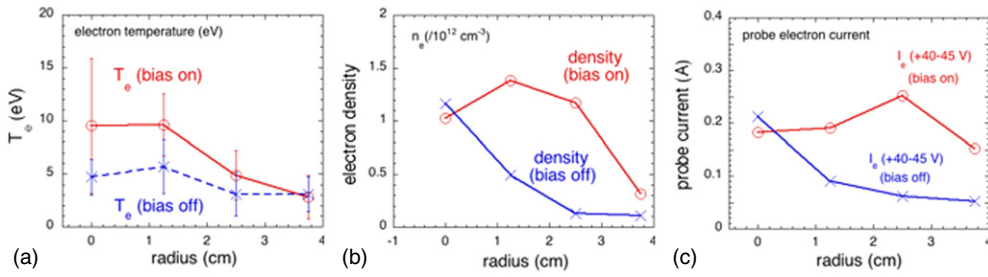
Figure 5. Effects of electrode biasing on the radial probe array. Plot (*a*) shows the electron temperature profiles inferred from the probe sweeps such as those in figure 4(*b*). The horizontal scale is the radial position of the probes in the radial array measured with respect to the first probe (#P3a), which is centered between electrode E2 and E3 (see figure 2). The T_e profiles show a slight increase in temperature with biasing. Plot (*b*) shows the electron density profiles inferred from the probe ion saturation currents and T_e measurements, which show a large increase with biasing in the outer three probes. Plot (*c*) shows the probe electron current profiles measured at +40–45 V, which also show a large increase with biasing in the outer three probes.

4.3. Radial profiles

All the radial profiles for probes in this paper are measured with respect to probe #P3a, which is centered between electrodes E2 and E3 (see figure 2). This probe is located ∼1.3 cm radially behind the 'shadow' of the nearby RF antenna (figure 1), so that all measurements are in the SOL of this antenna. The magnetic separatrix is typically located ∼2–10 cm radially inward from probe P3a, depending on the details of the plasma equilibrium.

Figure 5(*a*) shows the electron temperatures profiles inferred from probe sweeps like that of figure 4 by fitting an exponential curve through the part of the probe (I, V) characteristic near the floating potential. The electron temperatures were $T_e \sim 5$–10 eV averaged over 0.2–0.34 s for two similar shots (#129506, 129510), with a slight increase with the ±90 V biasing on. Figure 5(*b*) shows the electron density profiles n_e inferred from these same voltage sweeps using the conventional, but approximate, relation: $I_i = 0.5n_e A e c_s$, where the ion saturation currents I_i were averaged over −40 to −47 V, and the electron temperatures from figure 5(*a*) were used to calculate the sound speed c_s (e = electron charge, $A = 0.07$ cm^2). The density in the outer three probe channels clearly increases with the electrode biasing. Figure 5(*c*) shows the radial profiles of the probe electron current (at +40–45 V probe bias) during these same probe sweeps, labeled 'I_e(+40–45 V)'. The electron current in the outer three probe channels also clearly increases with the electrode biasing.

The changes in this electron current profile due to the electrode biasing seen in figure 5(*c*) are at least qualitatively similar to the changes in the electron density profile seen in figure 5(*a*), the difference between them being due to relatively small changes in the plasma potential and T_e during biasing. For example, an increase in the probe floating potential by ∼5 V during biasing, as seen in figure 4(*b*), will result in a ∼20% lower electron probe current at +45 V, even if there were no change in density or temperature. However, the large factor of ×3–5 increase in electron current seen in the outer probes during biasing in figure 5(*c*) must be dominantly due to changes in the local electron density.

For the results in sections 4.4–4.6, the variations in local plasma conditions due to electrode biasing were monitored by the electron currents measured by the probes at +50 V. It might be argued that the ion saturation current would have been a better measure of the local density changes, but the larger electron currents were needed for the fluctuation analyses of section 5, given the probe hardware limitations. For eventual application to control divertor plate heating,
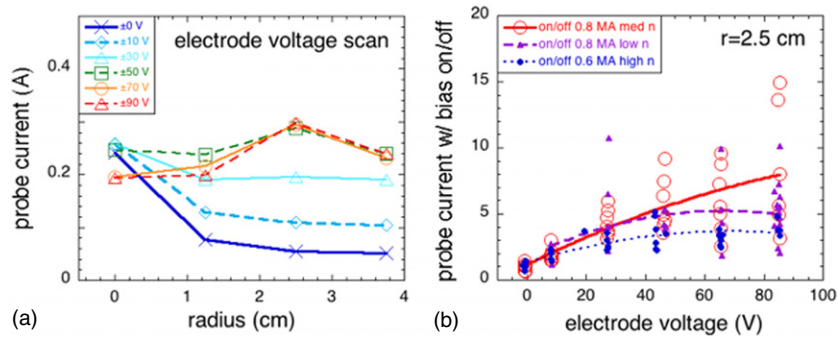
Figure 6. Variations with biasing voltage. Plot (*a*) shows the variation of the probe electron currents profiles (measured at +50 V probe bias) as a function of applied electrode bias voltage for a set of Ohmic discharges. The biasing was applied to electrodes E2 and E3 with equal and opposite voltage, with the $E_{pol} \times B$ drift direction outward between them. Plot (*b*) shows the ratio 'bias on' to 'bias off' probe electron current for three plasma conditions for the 2.5 cm probe. The lines in (*b*) are parabolic a fits to the corresponding points. There is a fairly large scatter in the results, but not much systematic variation with plasma conditions over this range.

the electron current may actually be a more relevant measure of the electrode biasing effect than the ion current.

4.4. Variation with electrode bias voltage

Figure 6 shows the effect of varying the electrode bias voltage on the radial profiles of probe electron currents (at +50 V probe bias). This figure shows the same result as figure 5: namely, a large and systematic increase in the SOL width of the probe currents signals due to electrode biasing.

Figure 6(*a*) shows that the effects of biasing start at about ±10 V and saturate in the range between ±50 and ±90 V. The plasmas used for figure 6(*a*) are the same Ohmic LSN plasmas (#129500–129505) used for figures 3–5. As for figures 3–5, there was a negative voltage on electrode E2 and an equal positive voltage on electrode E3, with the voltages 100% modulated in time and varied in magnitude from shot-to-shot, and electrodes E1 and E4 were grounded. The sign of the poloidal electric field between electrodes E2 and E3 was such that the resulting $E \times B$ drift direction was radially outward. The curves shown in figure 6(*a*) are the averages over ~0.2–0.34 s for each shot. There was very little shot-to-shot variation in the profiles during the 'bias off' times, as expected.

Figure 6(*b*) shows a larger set of data on the effects of the electrode bias voltage for the third radial probe ($r = 2.5$ cm) for 20 Ohmic shots within #129473–129505. The vertical axis is the ratio of probe electron currents (at +50 V probe bias) during each individual 'bias on' time period, divided by the corresponding signal during the 'bias off' time period. The red circled points are the same as those in figure 6(*a*) with $I = 0.8$ MA and $\langle n_e \rangle \sim 1.3 \times 10^{13}$ cm^{-3}, the purple triangles are shots with $I = 0.8$ MA and $\langle n_e \rangle \sim 0.7 \times 10^{13}$ cm^{-3}, and the blue solid dots are at $I = 0.6$ MA and $\langle n_e \rangle \sim 1.8 \times 10^{13}$ cm^{-3}. Each type of point is fit by a parabolic line. At an electrode bias of ±90 V the probe signal levels at $r = 2.5$ increased with biasing by roughly ×8 for these medium density cases, ×5 for the low density cases, and ×3–4 for the high density cases, with a fairly large scatter among the individual results.
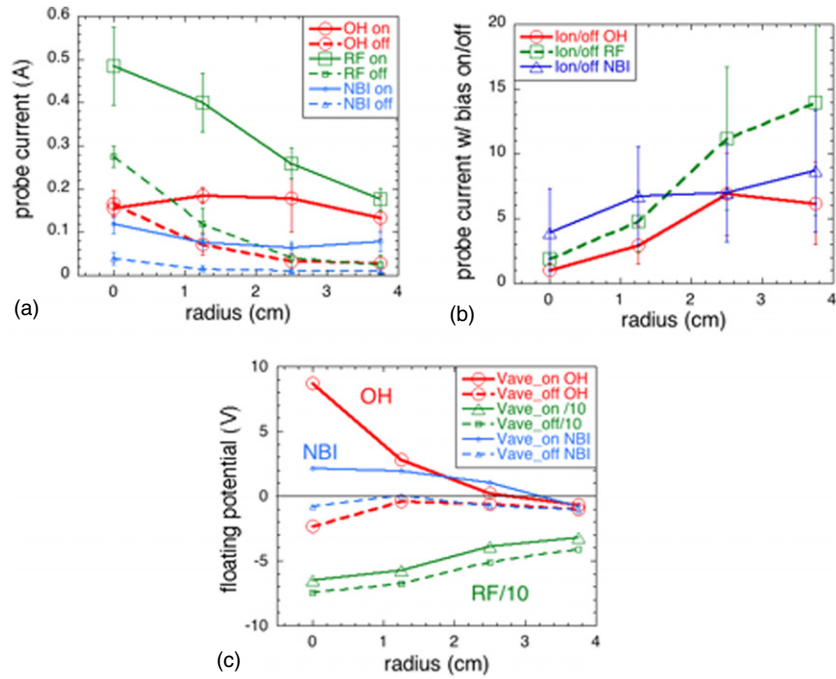
Figure 7. Electrode biasing effects for discharges with additional plasma heating. Plot (*a*) shows the electron current profiles (measured at +50 V probe bias) for 'bias on' and 'bias off' for Ohmic, RF and NBI plasmas, and plot (*b*) shows the ratios of the 'bias on' to 'bias off' probe currents at $r = 2.5$ cm. Plot (*c*) shows floating potential profiles with 'bias on' (solid lines) and 'bias off' (dashed lines) for OH, NBI and RF cases. The potentials increase with biasing by $\leqslant 10$ V, which is much smaller than the bias voltage of ± 50–90 V.

4.5. Variation with type of heating

Results for plasmas with other types of heating are shown in figure 7, where solid and dashed lines are the averages over all 'bias on' and 'bias off' periods during the steady-state plasma duration. The NBI cases have $P_{NBI} = 2$–4 MW, $B = 0.45$ T, $I = 0.8$ MA and $\langle n_e \rangle \sim 2.9 \times 10^{13}$ cm^{-3}, and $T_e(0) \sim 0.7$–1.0 keV, and the RF cases have $P_{RF} = 1$–2 MW, $B = 0.49$ T, $I = 0.65$ MA and $\langle n_e \rangle \sim 1.9 \times 10^{13}$ cm^{-3}, and $T_e(0) \sim 0.5$–0.7 keV. In all cases the B field angle near the outer midplane of $\sim 40°$ from horizontal (as is typical of spherical tokamaks).

Figure 7(*a*) shows that the SOL widths in the radial probe array become broader with electrode biasing for these three different cases: ± 90 V bias for Ohmic heated (OH) discharges, ± 90 V for neutral beam injection (NBI) discharges, and ± 50 V for high harmonic fast wave heated (RF). As in figures 3–6, the $E \times B$ drift direction was outward between electrodes E2 and E3. For the OH and RF cases electrodes E1 and E4 were grounded, while for the NBI cases electrode E1 was grounded and E4 was biased the same as E2. For the NBI plasmas the L-mode and H-mode behavior was similar, as described previously [27]. For all cases $I = 0.6$–0.8 MA and $B = 0.45$–0.55 T.

Figure 7(*b*) shows that the ratio of the probe electron currents (at +50 V probe bias) with the 'bias on' normalized to those with the 'bias off' is ~ 5–10 for the outermost probes. For OH plasmas the innermost probe current (P3a) changes very little or decreases with biasing, while for RF and NBI plasmas this probe current increases significantly. For OH plasmas the
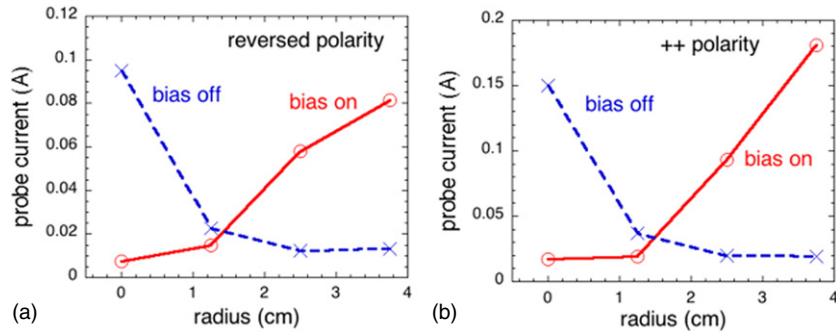
Figure 8. Effects of different electrode polarity. Plot (*a*) shows the electron current profiles (measured at +50 V probe bias) when the electrode polarity was reversed, i.e. with E2 positive and E3 negative (at the same voltage), so that the $E_{pol} \times B$ drift was radially *inward* at the probe array. Plot (*b*) shows the electron current profiles (measured at +50 V probe bias) when the electrode polarities of E2 and E3 were *both positive* (at the same voltage). The profiles with this biasing were similar to the reversed polarity case of plot (*a*), with the current in the outermost probe ∼10× that of the innermost probe.

radial profile during biasing is almost flat, while for RF and NBI plasmas the profiles fall with radius.

Figure 7(*c*) shows the floating potential profiles for these different types of plasmas. For OH and NBI, the floating potentials are near zero without biasing and become more positive with biasing, especially in the probes nearest the radius of the electrode location (i.e. $r \leqslant 1.25$ cm). For the RF case the floating potential is very negative without biasing due to the RF itself, but also becomes more positive with biasing. These changes in floating potential are all $\leqslant 10$ V and thus are much less than the applied bias voltages of ± 90 V for the OH and NBI cases and ± 50 V for the RF case.

4.6. Variation with electrode polarity and grounding

For all results so far the electrode E3 was biased positive and E2 negative with respect to the local vacuum vessel wall ground in order to create a local poloidal electric field outward $E \times B$ drift at the radial probe array. This section describes what happened when the polarity of these electrodes was varied.

Figure 8(*a*) shows the probe electron currents (at +50 V probe bias) when the electrode polarity was reversed, with E2 positive and E3 negative (at the same voltage), so that the $E \times B$ drift was radially *inward* at the probe array. These data were averaged over five NBI shots similar to those in figure 7 (#130092–130096), with 2 MW of NBI at $I = 0.8$ MA and $B = 0.55$ T. The E2, E3 electrode voltages were in the range of ± 50 to ± 90 V (as discussed above, the results are weakly dependent on voltage in the range), and electrodes E1 and E4 were grounded. In this case the radial profile strongly inverts with biasing, with the innermost probe signal being reduced by $\times 10$. This is an interesting and surprising result which can be explained to some extent by the effect of a convective cell rotation on the local radial profiles, as described in section 6.3. Figure 8(*b*) shows the probe electron currents (at +50 V probe bias) when the electrode polarities of E2 and E3 were *both positive* (at the same voltage). These data were averaged over six NBI shots similar to those in figure 8(*a*) (#130064–130071), with 3 MW of NBI at $I = 0.9$ MA and $B = 0.45$ T. The E2 and E3 electrode voltages were in the range of ± 50 to ± 70 V, and electrodes E1 and E4 were grounded. The results with this biasing
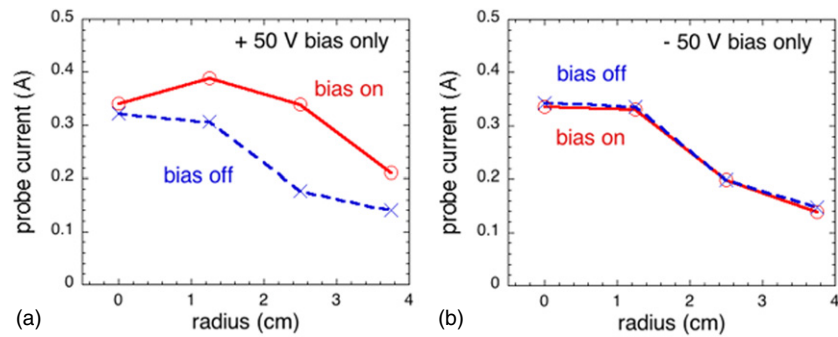
Figure 9. Effects of positive versus negative biasing. Plot (*a*) shows the electron current profiles (measured at +50 V probe bias) when E3 was +50 V and E2 was grounded (along with E1 and E4), while plot (*b*) shows the case when electrode E2 was −50 V and E3 was grounded (along with E1 and E4). The effects of biasing with only one electrode at +50 V were similar to those with ±50 V biasing (not shown), while the effects of biasing with only one electrode at −50 V were negligible.
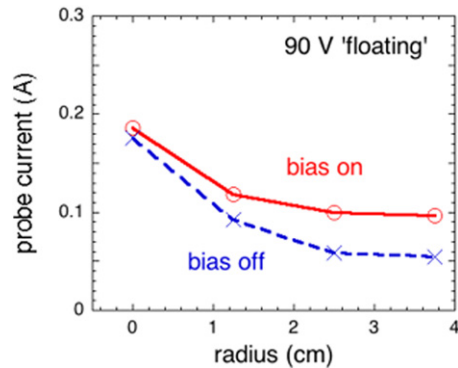

Figure 10. Effect of floating electrodes. The electron current profiles (measured at +50 V probe bias) are shown when electrode E3 was biased +90 V with respect to E2, so that the two electrodes E2 and E3 were floating with respect to ground (as in a double probe). The SOL profile is broadened, but considerably less than with the ±90 V biasing with respect to ground.

were similar to the reversed polarity case of figure 8(*a*), e.g. the current in the innermost probes decreased by about ×10 times with biasing.

Figure 9 shows the probe electron currents (at +50 V probe bias) when only *one* electrode was biased. For figure 9(*a*) electrode E3 was +50 V and E2 was grounded (along with E1 and E4), while for figure 9(*b*) electrode E2 was −50 V and E3 was grounded (along with E1 and E4). These data were averaged over two OH shots for each case (127165,166 or 127184,185), with at $I = 0.6$ MA and $B = 0.5$ T. The profiles with only one electrode at +50 V in figure 9(*a*) were similar to those at ±50 V biasing in this sequence of shots (not shown), while the profiles for −50 V only showed almost no change with biasing. Thus almost all the effects of biasing were due to the positive electrode, and almost no effects were due to the negative electrode. This is most likely due to different sheath effects for positive and negative biasing, as discussed in section 6.1.

Figure 10 shows the probe electron currents (at +50 V probe bias) when electrode E3 was biased +90 V with respect to E2, i.e. when the two electrodes E2 and E3 were floating with respect to ground (as in a double probe), while electrodes E1 and E4 were grounded.
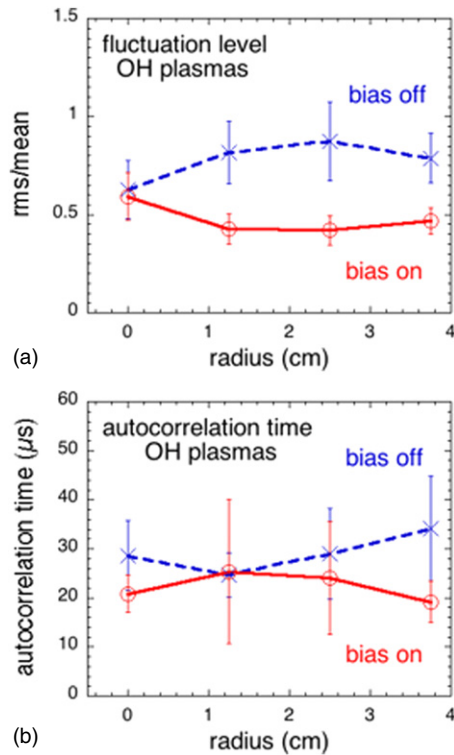
Figure 11. The effect of biasing on the relative probe current fluctuation levels and autocorrelation times for a set of Ohmic discharges with normal biasing (radial $E \times B$ drift outward). The relative fluctuation levels show a systematic decrease by up to $2\times$ in the radial regions where the local density was increased with biasing (as in figure 5). The autocorrelation times are slightly decreased by the biasing.

This configuration was of interest because the current (and power) drawn by the electrodes was significantly lower than when the electrodes were biased with respect to the wall (see figure 4(*a*)). These data were averaged over the steady-state portion of four OH shots (#129402–129407). These profiles show a local broadening of the SOL with biasing, with a profile-averaged e-folding length of 3.2 cm with 'bias off 'compared with 5.8 cm with 'bias on'. However, this change is significantly less than with the ±90 V biasing with respect to ground of figure 6(*a*).

5. Effects of biasing on turbulence and other results

Section 4 described the effects of electrode biasing on the time-averaged radial profiles as measured by the probes between the biased electrodes. This section describes measurements of turbulence and other results obtained during these same biasing experiments.

5.1. Effects on the local turbulence

Figures 11 and 12 show the effects of electrode biasing on the turbulence measured by the radial probe array between electrodes E2 and E3 (#P3a-P3d). For these data the bias level was ±70 or ±90 V with respect to vessel ground in the 'normal' direction for Ohmic plasmas,
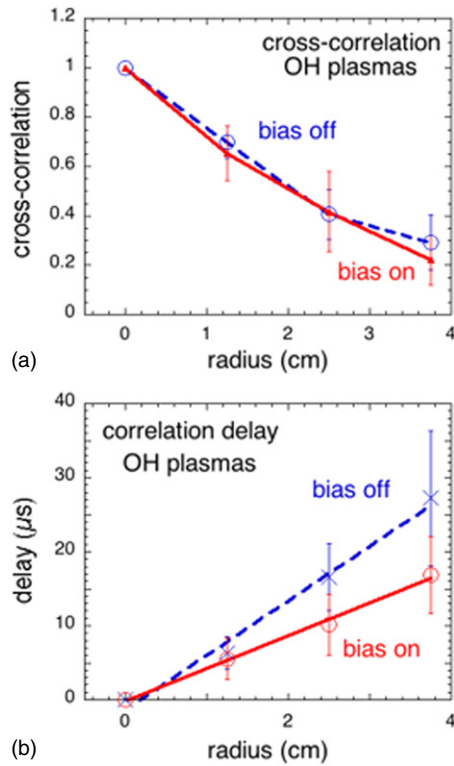
Figure 12. The effect of biasing on the cross-correlations between the probe at $r = 0$ cm and the other probes in the radial array. The biasing has no effect on the radial cross-correlation coefficients. There was a small increase in the outward radial propagation speed with biasing from $\sim$1.4 to $\sim$2.3 km s^{-1} (i.e. a decrease in slope).

i.e. with the radial $E \times B$ drift outward. The fluctuations were measured in the probe electron currents (at +50 V probe bias) for eight Ohmic plasmas in the data set of figure 6.

The relative fluctuation levels without biasing are in the range $\sim$30% to 90% (rms/mean), as usual for SOL turbulence in NSTX and other tokamaks, as shown in figure 11(*a*). These relative fluctuation levels show a systematic decrease by up to 2$\times$ in the radial regions where the time-averaged local density was increased with biasing, as in figures 5 and 6. The autocorrelation times (i.e. the time for the autocorrelation function to reach 0.5) as shown in figure 11(*b*) are in the range $\sim$20–40 μs, also similar to previous NSTX SOL measurements. The profile-averaged autocorrelation times are $30 \pm 4 \, \mu$s with 'bias on' and $22 \pm 3 \, \mu$s with 'bias off', thus showing a marginally significant decrease with biasing.

The zero-time-delay cross-correlation coefficients between the probe at $r = 0$ cm and the other probes in the radial array are shown in figure 12(*a*). The radial correlation length is $\sim$4 cm (FWHM), as in previous NSTX SOL measurements. The biasing has no significant effect on the radial cross-correlation coefficients. The radial turbulence speed also was determined from the delay time of the peak in the cross-correlation between the probe at $r = 0$ cm and the other probes, as shown figure 12(*b*). Without biasing the turbulence propagated predominantly in the radially outward direction, as usual for the NSTX SOL [29]. There was an increase in the profile-averaged outward radial propagation speed with biasing from $\sim$1.4 to $\sim$2.3 km s^{-1}. No statistically significant differences in the radial turbulence speed with 'bias on' versus 'bias
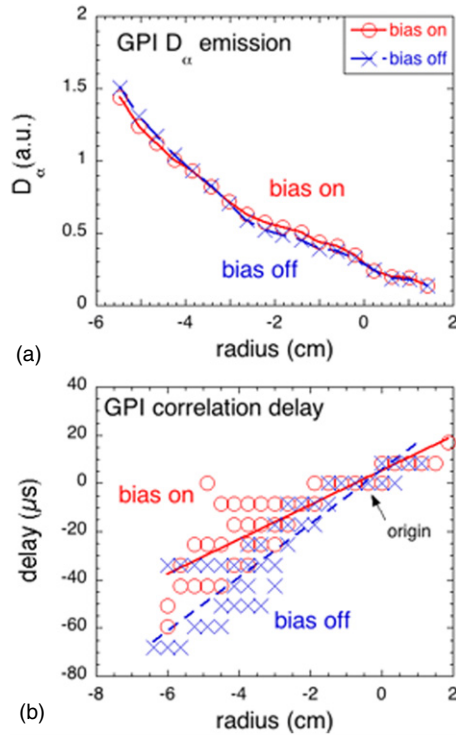
Figure 13. Effects of biasing on the GPI diagnostic. Plot (*a*) shows the radial profile of the average D_α light seen by the GPI diagnostic at the same poloidal location as the probe array over -6 to $+2$ cm with respect to the $r = 0$ cm probe location. There was no measurable perturbation due to the electrode biasing in this D_α profile. Plot (*b*) shows the delay times of the peak of the cross-correlation function versus radius for the turbulence propagation, as for figure 12(*b*). There was a slight increase in the outward radial propagation speed with biasing (i.e. a decrease in slope), but only slightly outside the measurement uncertainty.

off' was measured in cases with NBI or with reversed polarity, but the number of bias cycles was lower and the statistical variations larger than for figure 12(*b*).

5.2. GPI results

The GPI diagnostic location is shown in figure 1 and was described briefly in section 3. The radial and poloidal profiles of the D_α emission from the GPI gas cloud were measured $\sim$1 m along B from the biased electrodes. In the range of interest for this experiment ($n \sim 10^{11}$– 10^{12} cm^{-3}, $T_e \sim 5$–10 eV), the average D_α emission should be linear with density and roughly proportional to T_e^{1-2}, although the exact dependences are not measured. The fluctuations in D_α emission will depend on both the n and T_e fluctuations.

The GPI images were spatially aligned with the electron current signals from the Langmuir probes of figure 2 by cross-correlating their turbulent fluctuations. The maximum cross-correlation coefficient between the GPI and the probe P3a was $\sim$0.75–0.78, so these two diagnostics responded very similarly to the same turbulent 'filaments', which are well known to have a large correlation length along B. A 2D image of the cross-correlation coefficients showing good alignment of all five probes was shown in [26].

Using this alignment, the radial profile of the average D_α light along the radius of the probe radial array is shown in figure 13(*a*) for one shot (#127054), which was one of the NBI

14
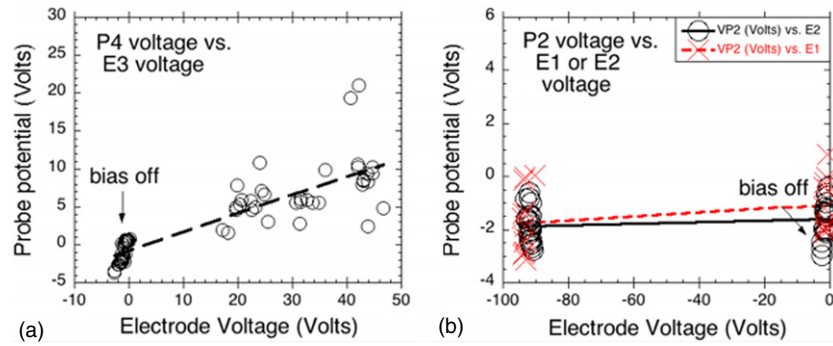
Figure 14. Effects of positive and negative biasing on the floating potential. Plot (*a*) shows the floating potential measured on probe #P4 as a function of the positive voltage in the adjacent electrode #E3 when the electrode on the other side of this probe (#E4) was grounded. The floating potential on the probe next to this positively biased electrode changes by ∼10–20% of the applied electrode voltage. Plot (*b*) shows the floating potential measured on probe #P2 as a function of the negative voltage in the adjacent electrode #E3 or #E1 when the electrode on the other side of this probe was grounded. In these cases the floating potential on a probe next to a negatively biased electrode does not change significantly.

shots of figure 7. The radial scale goes from -6 to $+2$ cm with respect to the $r = 0$ cm probe location (outside of which the D_α signal level was too small to be reliably measured). The radial profiles during 'bias on' times were negligibly different from the adjacent 'bias off' times, as were the poloidal profiles. Thus there was no measurable effect on the time-averaged D_α emission profiles at the GPI location due to the electrode biasing. This suggests that the electrode biasing does not affect the plasma ∼1 m along B, as discussed in section 7.2.

The GPI signals along this same radial axis for the same shot were used to calculate the delay times of the peak of the cross-correlation function versus radius for the turbulence propagation, just as for figure 12(*b*). The resulting delay times are shown in figure 13(*b*) for the same data set as for figure 13(*a*). There was a small increase in the outward radial propagation speed with biasing from ∼0.9 to ∼1.3 km s^{-1}, but only for $r < 0$. There were only small changes in the autocorrelation times (26 ± 3 μs with 'bias on' versus 17 ± 3 μs 'bias off'), the radial correlation lengths (3.8 ± 0.3 cm FWHM with 'bias on' versus 2.8 ± 0.3 cm FWHM 'bias off'), and the poloidal correlation length (3.6 ± 0.4 cm FWHM with 'bias on' versus 5.0 ± 0.5 cm FWHM 'bias off').

Thus the GPI diagnostic located ∼1 m along B from the electrodes showed no significant change in the time-averaged profiles and only small changes in the turbulence with biasing in this experiment. The most likely interpretation is that the parallel perturbation length of the biasing was <1 m in this experiment, as discussed in section 7.2.

5.3. Floating potential variation with electrode voltage

Figure 14(*a*) shows the floating potential changes at a probe adjacent to a positively biased electrode. Here the floating potential on probe #P4 is plotted against the voltage on electrode #E3 for four shots in which the electrode on the other side of this probe (i.e. #E4) was grounded. These data were for four Ohmic plasmas with $I = 0.8$ MA and $B = 0.45$ T (#124679–124688), similar to those used for figures 6 and 7(*c*). Each point represents the average value in one 'bias on' or 'bias off' period. The floating potential on #P4 typically increases by +5–10 V for an E3 electrode voltage of +20–50 V. Thus the floating potential on the probe next to a positively biased electrode changes by ∼10–20% of that electrode voltage.

15
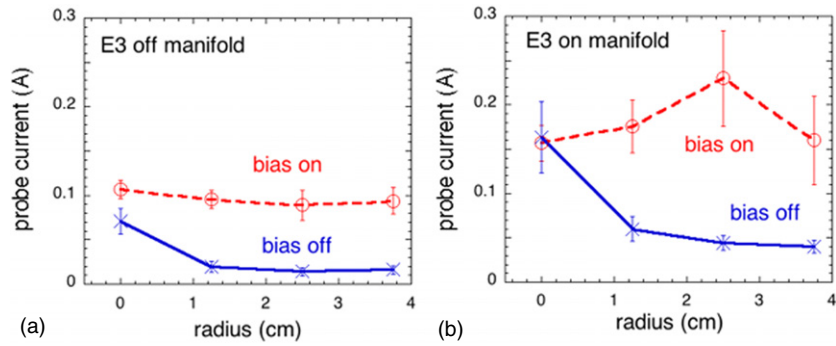
Figure 15. Effect of the gas manifold field line connection on the radial profile of the probe electron current profiles (at +50 V probe bias) with and without biasing. The biasing was applied to electrodes E2 and E3 with the $E_{pol} \times B$ drift direction outward between, as in figure 6. Case (*a*) was when the field lines from electrode E3 were not connected to the gas manifold and case (*b*) was when the field from electrode E3 were partially connected to the manifold. The effect of biasing is at least qualitatively similar between these two cases.

Figure 14(*b*) shows the floating potential changes at a probe adjacent to a negatively biased electrode (note change in vertical scale from figure 14(*a*)). Here the 'O's' are the floating potential on probe #P2 versus the voltage on electrode #E2 for shots in which the electrode on the other side of this probe (i.e. #E1) was grounded. The 'x's' are the floating potential on probe #P2 versus the negative voltage in the adjacent electrode #E1, for shots in which the electrode on the other side of this probe (#E2) was grounded. In both cases the floating potential on a probe next to a negatively biased electrode does not change. This is consistent with the absence of SOL changes for a negatively biased electrode (figure 9).

There is considerable scatter in the floating potential response to the positive bias as shown in figure 14(*a*), the origin of which is not understood at present. There was no clear correlation between these floating potential changes and the current drawn by the positive electrode E3 in these cases.

5.4. Effect of GPI gas manifold

In this experiment the electrodes and the GPI diagnostic were intentionally aligned along a field line to try to measure the effects of the biasing along B. However, this sometimes (depending on the details of the plasma equilibrium) put the GPI gas puff manifold on B field lines which were connected to the electrodes. The GPI gas manifold was a stainless steel tube grounded to the vessel, so in principle this grounding could affect the flow of current and the potential in the electrode flux tube.

Figure 15 shows a check of this effect made by comparing two cases for ± 90 V biasing shots like those in figure 3: (a) near the end of the current ramp-up phase ($\leqslant 0.11$–0.15 s) when all the field lines from electrode E3 were at least 1 cm radially inside and 1 cm radially below the manifold, and (b) during the steady current phase (0.2–0.3 s) when about half of the field lines from electrode E3 were intersecting the manifold (according to the equilibrium code EFIT). The result is that the currents in the outer three probes increased by a factor of $\sim 5.7 \pm 0.8$ with biasing when the electrode was off the manifold, compared with $\sim 4.1 \pm 1.1$ when the electrode was on the manifold, i.e. the increase was similar in both cases. This shows that a change in the electrical connection to ground ~ 1 m downstream from the electrodes along B does not significantly change the SOL modification near the electrodes.

16

6. Comparisons with the theoretical models

Section 6.1 compares the experimental results with the theory of divertor plate biasing, while section 6.2 compares the results with other theories for the parallel and perpendicular penetration lengths of the bias potential. Section 6.3 describes a simple convective cell model for the expected SOL modification and compares it with the experimental results.

6.1. Comparison with theory divertor plate biasing

This experiment was motivated by the theories of convective cell generation by divertor plate biasing [5–7]. Some of this theory is relevant to the present experiments at the outer midplane, even though the specific divertor physics issues are not relevant.

   The initial paper [5] proposed creating convective cells with divertor plate biasing. The condition for convective cell formation was that the plasma potential change due to biasing was larger than the unperturbed radial potential variation across the cell. This appears to be the case in these experiments, since the floating potential change due to positive biasing, as shown in figures 7(c) and 14(a), was larger than the unbiased potential gradient, as shown in figure 7(c), at least over $r = 0$ to 2 cm for the OH and NBI cases. Reference [5] also compares the expected convective cell radial transport to Bohm diffusion. However, the SOL transport in NSTX is likely dominated by turbulent 'blobs' with a typical radial speed of $\sim$1 km s^{-1} [29]. For the NSTX experiments, the bias-induced convective cell transport (i.e. radial flow speed) would be larger than this blob transport for $E_{\mathrm{pol}} > 2.5$ V cm^{-1}, which is likely to be the case since typical potential changes in the probes were $\sim$5–10 V at a distance of 0.5 cm from the electrodes (although the local poloidal field was not directly measured). A final point in [5] is that the parallel voltage drop due to the plasma resistance could 'consume' the bias potential if T_{e} was too low. However, for the present experiment with $T_{\mathrm{e}} \sim 8$ eV (figure 5(a)) and $j_{\parallel} \sim 10$ A/10 cm^2 (for positive biasing), the resistive voltage drop is only $\leqslant 1$ V/100 cm, which is only $\sim$1% of a 100 V bias voltage over the $\sim$1 m parallel scale of interest in this experiment.

   A second paper [6] discussed in more detail the sheath physics for biased plates. Assuming a model in which the electrode current flows along a magnetic flux tube of constant area to a grounded plate far along B, it was shown that for *negative* biasing the plasma potential in this tube would not exceed $\sim$0.8T_{e}/e, whereas for *positive* biasing the plasma potential (with respect to ground) would increase by $\sim T_{\mathrm{e}}/e \ln[\{\exp(e\varphi_{\mathrm{b}}/T_{\mathrm{e}}) + 1\}/2]$, where φ_{b} is the plate bias potential ($\sim$100 V in these experiments). For the present SOL where $T_{\mathrm{e}} \sim 8$ eV and $e\varphi_{\mathrm{b}}/T_{\mathrm{e}} \sim 10$, this implies that the plasma potential should change by about -8 V with negative bias and by $+90$ V with positive bias. This degree of asymmetry is at least qualitatively consistent with the asymmetrical SOL modification results of figure 9, although the measured potential changes in figures 7(c) and 14(a) are significantly smaller than these. The large ratio of positive to negative electrode current of $\sim$8 of figure 4(a) shows that the effective area of the 'downstream' current path is significant larger than the electrode area in this experiment. This is modeled in that paper by an area ratio A, which is the effective area for the downstream electrode normalized to the area of the biased electrode ($A = 1$ for a symmetrical double probe model). However, for the observed $A = 8$ the expected negative plasma potential goes to $\sim$80 V, which is not significantly different from the case for $A = 1$.

   A third paper in this series [7] further discussed symmetry of positive versus negative biasing through a model of divertor plate biasing which allowed cross-field currents near the X-point. Although this geometry is not relevant to the present experiment, the generic effect of cross-field currents is to reduce the potential changes for the positive bias to the same level of those for negative bias. In the present experiment the asymmetrical electrode (I, V)

17

Table 1. Theoretical estimates for bias penetration.

$n = 10^{12} \, \text{cm}^{-3}$ (assumed electron density)
$T_e = 8 \, \text{eV}$ (assumed electron temperature)
$n_o = 10^{12} \, \text{cm}^{-3}$ (assumed neutral density)
$M_i = 2$ (assumed ion mass)
$\lambda_D \sim 10^{-3} \, \text{cm}$ (Debye length)
$\lambda_{mfp} \sim v_e/v_{ie} \sim 60 \, \text{cm}$
$\lambda_{Spit} \sim \sigma_\parallel T_e/(ne^2 c_s) \sim 5 \times 10^3 \, \text{cm}$
$L_\parallel \sim \lambda_{mfp}(M_i/m_e)^{1/2} \sim 3 \times 10^3 \, \text{cm}$
$R_{visc} \sim \rho_{ci}(M_i/m_e)^{1/8}(\mu/\rho_{ci}^2 \nu_{ii})^{1/4} \sim 1.1 \, \text{cm}$
$R_{inert} \sim \rho_{ci}[(u_d/c_s)(\lambda_{e,coll}/\rho_{ci})(M_i/m_e)^{1/2}]^{1/3} \sim 1.6 \, \text{cm}$
$R_{neut} \sim \rho_{ci}(\nu_{iN}/\nu_{ii})^{1/2}(M_i/m_e)^{1/4} \sim 0.8 \, \text{cm}$

characteristic (figure 4(*a*)) implies that there are cross-field currents, but their effect is not large enough to make the response symmetric with respect to plus and minus biasing (figure 9).

These papers also discuss the possibility of turbulence generation due to the shear flow in bias-induced convective cells; however, in the present experiment the turbulence level was already high without biasing, and *decreased* with biasing (see figure 11(*a*)), so it is unlikely that the biasing created additional turbulence. References [6, 7] also calculated the heat load on the plates due to biasing, which in the present experiment is only $\sim 10 \, \text{A} \times 100 \, \text{V} \sim 1 \, \text{kW}$.

The effects of positive and negative biasing in this experiment are different from those for the TEXTOR biased limiter experiments, as described by Gravier in [14]. In that work, a positive bias was not effective in creating a radial electric field because a part of the current was returned along B field lines to the grounded inner bumper limiter. In the present experiment there was no clear current path to ground along B, so the positive bias could more easily create a positive plasma potential in the plasma (at least near the electrodes). Note that the actual electric fields and current paths in the plasma were not directly measured in this experiment, so that interpretation of the SOL profile results can only be made through modeling, such as described below.

6.2. Penetration lengths of the bias potential

The parallel and perpendicular scale lengths for the penetration of a biased electrode potential into a SOL plasma was discussed by Rozhansky [21] and Carlson [22]. Table 1 shows an evaluation of these scale lengths for the present experiment.

The parallel penetration length from [21] was estimated to be $\sim 3 \times 10^3 \, \text{cm}$, which is about the same as the parallel resistive scale length λ_{Spitz} [22]. This appears to be inconsistent with the absence of a clear perturbation due to electrode biasing at the GPI diagnostic $\sim 1 \, \text{m}$ along B, but this may be due to the neglect of turbulent cross-field transport in the model, as discussed in section 7.2.

The perpendicular penetration lengths for the electrode potential was evaluated from [21] assuming either viscous, inertial or ion-neutral friction and associated cross-field conductivity. For this experiment these lengths are all $\sim 1 \, \text{cm}$, as shown in table 1. For these evaluations, the anomalous viscosity μ was taken to be Bohm, and the radial flow speed u_d was taken to be the typical 'blob' speed of $1 \, \text{km} \, \text{s}^{-1}$, and a typical SOL neutral density of $n_o \sim 10^{12} \, \text{cm}^{-3}$ was assumed. These perpendicular scales are comparable to the radial potential scale length of ~ 1–$2 \, \text{cm}$ seen in figure 7(*c*), and with the small potential change at the probe $\sim 0.5 \, \text{cm}$ from the electrode, as in figure 14(*a*). However, the Rozhansky model assumed that the electrode
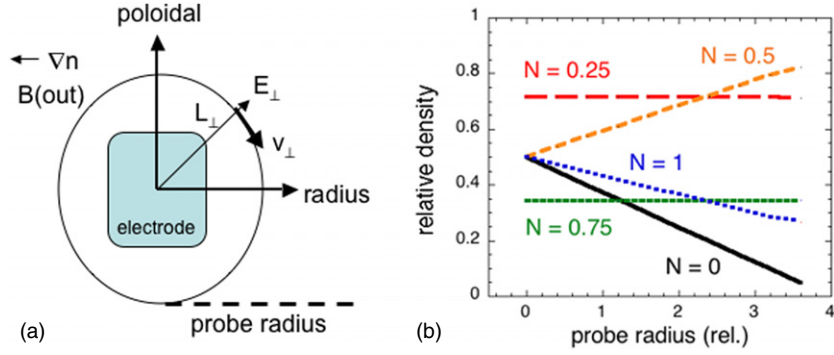
Figure 16. Model for the effects of biasing on the SOL profile. Part (*a*) shows a sketch of the geometry, where the magnetic field *B* is out of the paper, the electrode is in the radial versus poloidal plane perpendicular *B*, and the density gradient (without bias) is in the radial direction. Plot (*b*) shows the profiles for various convective cell rotations *N* for an initial profile (*N* = 0). These profiles are plotted for a poloidal location 2 units below the rotation axis, in the direction corresponding to outward $E_{pol} \times B$ flow.

bias did not significantly perturb the density along the field line, and that the probe current is significantly below electron saturation, which may not be the case for this experiment.

If, indeed, the parallel penetration length of the potential in this experiment was <1 m, this suggests that the cross-field currents were much larger than those estimated above. There is presently no clear experimental indication of the cause for such currents. Although in previous radial biasing experiments the neutral friction was considered to be an important mechanism for the radial current [8, 9], for this experiment the estimated perpendicular ion-neutral conductivity $\sigma_{\perp} \sim 10^{-3}\,\Omega^{-1}\,m^{-1}$ implies a negligible cross-field current of <1 A at ~100 V bias over ~1 m of the electrode flux tube.

6.3. Relationship of $E \times B$ flow to SOL profile modification

The theory discussed in sections 6.1–6.2 did not describe how the radial profiles of SOL density should be affected by the electrode biasing. This section describes a simple model which illustrates how these $E \times B$ flows could be related to their expected effects on the local SOL. This model can at least qualitatively explain some of the SOL profile modifications due to biasing shown in figures 6–8.

Assume the simplified biasing geometry of figure 16(*a*). The magnetic field *B* is in the direction out of the paper, the electrode is in the radial versus poloidal plane perpendicular *B*, and the density gradient (without bias) is in the radial direction. The biased electrode creates a perpendicular electric field $E_{\perp}$ surrounding the electrode at a distance $L_{\perp}$ from its center, which extends in one direction along *B* by a distance $L_{\parallel}$. The plasma within this convective cell of length $L_{\parallel}$ also flows along *B* with a parallel speed $v_{\parallel}$, and drifts across *B* with a perpendicular speed $v_{\perp} = E_{\perp} \times B_z$ over $L_{\parallel}$. If this $E_{\perp} \times B_z$ drift is the only mechanism for plasma transport across *B*, the number of plasma rotations *N* around *B* over a parallel transit time $(L_{\parallel}/v_{\parallel})$ along the convective cell is

$$N = v_{\perp}(L_{\parallel}/v_{\parallel})/(2\pi L_{\perp}). \tag{1}$$

Thus *N* depends upon the parallel and perpendicular penetration lengths, as well as the parallel and perpendicular velocities. For example, if $L_{\parallel} \sim 50$ cm (half the distance to the GPI), $L_{\perp} \sim 3$ cm (based on figure 7(*c*)), $v_{\parallel} \sim 10^6$ cm s^{-1} (corresponding to a parallel Mach speed of
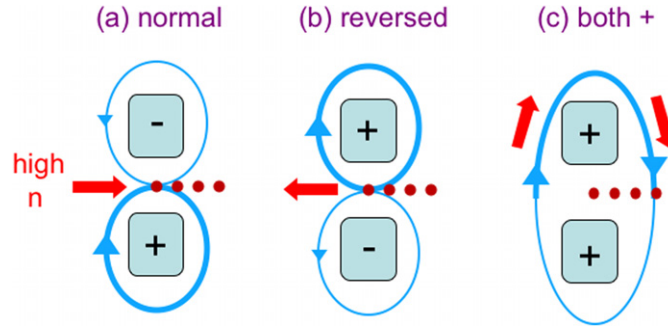
Figure 17. Qualitative picture of the expected $E \times B$ flow patterns for various biasing configurations of electrodes E2 and E3 (squares), along with the radial probe array (dots), with the radially outward direction to the right. Case (*a*) is for normal polarity (outward $E_{pol} \times B$ flow between the electrodes), case (*b*) is for reversed polarity and case (*c*) is for both electrodes positive. The dark circles show the expected flow due to the positively biased electrode, which is presumed to be dominant, and the light circles show the expected flow due to the negatively biased electrode, which had almost no effect (figure 9).

$M_{\parallel} \sim 0.5$ at 8 eV) and $v_{\perp} \sim 4 \times 10^5$ cm s^{-1} (corresponding to $E_{\perp} = 10$ V cm^{-1} at $B = 0.25$ T), then $N \sim 1$.

An example of the effect of various convective cell rotations N on an initial local density profile is shown in figures 16(*b*). The horizontal axis is the 'probe radius' as measured along the dotted line below the electrode in figure 16(*a*), and the vertical axis is the relative density profile for various N, including the unbiased case $N = 0$. This model assumes a rigid-body rotation of the plasma in the $E_{\perp} \times B$ direction, along with some spread in $v_{\parallel}$ to simulate a parallel thermal ion distribution. The initial density profile ($N = 0$ case) is assumed to be constant in the poloidal and z directions and linear over eight radial units (± 4 units on either side of the rotation axis).

To simulate convective cell rotation with various N, this initial density profile is rotated around the origin of figure 16(*a*) in successive steps. The resulting radial profiles at the 'probe radius' line versus N are plotted in figure 16(*b*) for a poloidal location 2 radial units below the rotation axis, which is the 'outward' $E \times B$ flow direction in this model. A rotation of $N = 0.25$ flattens the radial profile and raises its level, because this was previously the poloidal distribution at $r = -2$ units. A rotation of $N = 0.5$ inverts the radial distribution, since this was previously the distribution along the negative radial direction. A rotation of $N = 0.75$ flattens the radial profile and lowers its level, because this was previously the poloidal distribution at $r = +2$ units, and a rotation of $N = 1$ brings back the distribution of $N = 0$, except for a radial flattening due to the assumed spread in parallel rotation speeds. For large $N \gg 1$, the radial distribution becomes flat at a level of 0.5 due to this spreading.

This model can be related to the experimental results of section 4 by considering the expected $E \times B$ flow patterns as shown in figure 17. This figure shows electrodes E2 and E3 along with the radial probe array, with the radially outward direction to the right. The dark circles show the expected flow due to the positively biased electrode, which is assumed to be dominant, and the light circles show the expected flow due to the negatively biased electrode, which has almost no effect (figure 9). For the 'normal' biasing case of figure 17(*a*), the radial $E \times B$ flow is outward at the probe array, and so the model results of figure 16(*b*) can be compared with the experimental profiles of figure 6(*a*). The measured profiles first flatten up about ± 50 V, and then partially invert at up to ± 90 V. The closest qualitative fit to the model

20

seems to $N \sim 0.25$ at ± 50 V and $N \sim 0.5$–0.75 at ± 90 V. For other experimental cases, such as for NBI and OH in figure 7(a), the profiles flatten at a higher level, similar to the model for $N = 0.25$.

The results of the model for a poloidal location above the rotation axis, which is the direction for 'inward' $E \times B$ flow, are the same as figure 16(b) except that the $N = 0.25$ and $N = 0.75$ labels are switched. This can be compared with the experimental results for the 'reversed' polarity in figure 8(a), where the expected flow directions are indicated in figure 17(b). The closest qualitative fit to the model seems to be at $N \sim 0.5$, but the model does not explain the very low signal seen at $r = 0$ cm in the reversed bias case. The result of figure 8(b) when *both* electrodes were positive could be qualitatively interpreted either in terms of one clockwise convective cell around each of the electrodes, or one large clockwise convective cell around both electrodes, as illustrated in figure 17(c). An increase in the flux to the outermost probe at $r = 3.75$ cm might also be expected if this flow went around the electrodes as shown in figure 17(c). If so, the closest fit to the model would again be the $N \sim 0.5$ case of figure 16(b).

Thus a simple convective cell rotation of $\sim 90°$–180° (i.e. $N \sim 0.25$–0.5) can at least qualitatively explain the observed flattening and/or inversion of the radial profiles with biasing in figure 6–8. However, this model could not explain the strong reduction in the electron current seen at the $r = 0$ location in figure 8, or the similarity of the results for the two different bias cases of figure 8. To obtain a successful quantitative model it would be necessary to incorporate the actual radial profiles (including at $r \leqslant 0$) for the unbiased case, the full 2D (or even 3D) flow pattern set up by the biasing and the possible effects of these flows on the plasma transport into and across the convective cell. Since these were not measured in this experiment, such modeling is beyond the scope of this paper.

7. Summary and discussion

7.1. Summary of experimental results

In this experiment a local poloidal electric field created by electrode biasing with respect to the vessel wall in order to control the local SOL profiles in NSTX. These small electrodes did not (and were not designed to) affect the global plasma parameters. The main experimental results are summarized below, and the theoretical interpretations are discussed in section 7.2.

(1) the local electron probe current and floating potential profiles were strongly modified by a pair of ±biased electrodes which created a local electric field in the poloidal direction (figures 6–8),

(2) the radial width of the SOL profile increased when the $E \times B$ drift due to these electrodes was directed outward, but the SOL profile inverted for an inward $E \times B$ drift or for a positive polarity on both electrodes (figure 8),

(3) these changes are predominantly caused by the positively biased electrode, with almost no changes due to the negatively biased electrode (figures 9 and 14), which differs from some previous divertor biasing experiments, e.g. those on TEXTOR (see section 6.1),

(4) the local turbulence between these electrodes and the D_α profiles and turbulence measured ~ 1 m downstream from the electrodes were not significantly affected by this biasing (figures 11–13),

7.2. Theoretical interpretations

A simple convective cell model of the theoretically-expected flows due to $E \times B$ drifts as discussed in section 6.3 at least partially explains the flattening and slight inversion of the SOL profiles during 'normal biasing' in this experiment. However, quantitative modeling of these profile changes would require knowledge of the parameters which were not directly measured, such as the parallel and perpendicular penetration lengths of the bias potential (see equation (1)). Thus, for example, there is at present no quantitative theoretical understanding of the variation with electrode voltage (figure 6), or the similarity between the results for reversed and doubly-positive biasing (figure 8), or for the relatively small effect with floating electrodes (figure 10).

The strong asymmetry observed between the effects of positive and negative biasing were predicted by the modeling of [5–7], as discussed in section 6.1. This is due to the large voltage drop expected across the thin sheath in front of the negative electrode ($\lambda_D \ll 0.1$ cm). However, the magnitude of potential changes measured adjacent to the positive electrode (e.g. figure 14(*a*)) were less than predicted by this theory. These potentials could possibly be explained by a small perpendicular scale for the potential penetration (<1 cm), as estimated in section 6.2.

The most direct measurement of the effect of biasing on the $E \times B$ drifts in this experiment was the radial propagation speed of the turbulence, which should have increased due to the locally outward $E_{pol} \times B$ drift velocity. There was a marginally significant $\sim 1 \, \text{km s}^{-1}$ increase in the measured radially outward turbulence velocity in the probe array with outward $E \times B$ biasing (figure 12(*b*)), but this was far smaller than the expected effect of the full applied $E_{pol} \times B$ drift (e.g. $v_{rad} \sim 20 \, \text{km s}^{-1}$ at $50 \, \text{V cm}^{-1}$). There was also a marginally significant $\sim 0.4 \, \text{km s}^{-1}$ increase in the radially outward turbulence velocity at the GPI location (figure 13(*b*)). Although these changes were small, they are not inconsistent with the relatively small number of convective cell rotations ($N \sim 0.5$) inferred from the model of section 6.3. The relatively small magnitude of these $E_{pol} \times B$ drifts has not yet been explained by theory.

The large ratio of the electron to ion current drawn by the electrode, as shown in figure 4(*a*), indicates that there is a significant cross-field current in this experiment, as usual for probes or electrodes in tokamaks. The origin of this cross-field current is not understood. This anomalous cross-field current may have caused the relatively small response observed with the 'floating electrodes', as shown in figure 10, since the current path from positive to negative electrodes is shorter than from the positive electrode to the vessel ground, which could reduce the parallel penetration length of the potential.

The most surprising experimental result was the negligible effect of the biasing on time-averaged D_α profiles and turbulence as seen in the GPI diagnostic ~ 1 m along B, as discussed in section 5.2. This is evidence that the near-dc perturbation due to the electrode biasing did not penetrate ~ 1 m parallel to the B field, even though the turbulence measured in the GPI diagnostic was highly correlated with the turbulence measured in the probes near the electrodes. A similar result was obtained in TEXT [18], where the ion saturation current perturbation due to a positively dc biased probe located 12 m. along B was much less distinct than the perturbation due to a 30 kHz oscillating bias. Further evidence for this parallel locality of the biasing comes from the minimal effect of differing electrical grounding at the gas manifold, as discussed in section 5.4.

This evidence for a highly localized parallel perturbation appears to be inconsistent with the large parallel scale lengths predicted by the theory of section 6.2. However, this theory was done for a quiescent plasma and did not include the effects of SOL turbulence, which could modify the local cross-field transport as the perturbation travels along B. For example, a

'blob' with a radial speed of $\sim 1 \,\mathrm{km\,s^{-1}}$ would move $\sim 10 \,\mathrm{cm}$ over the timescale of parallel ion transport over $1 \,\mathrm{m}$ (i.e. $1 \,\mathrm{m}/10^6 \,\mathrm{cm\,s^{-1}} \sim 10^{-4} \,\mathrm{s}$), which is larger than the radial perturbation size in this experiment. A theoretical analysis of such turbulence effects is beyond the scope of this paper.

7.3. Possibilities for further investigation

The next step for this experiment would be to install electrodes in the divertor plates to determine how well this type of biasing can control the SOL plasma near the divertor strike zone. Plans are underway to install several electrodes on future divertor tiles in NSTX. Further experiments at the outer midplane could have movable electrodes and a way to vary their size or shape.

On the diagnostic side, the biggest improvement would come from an increase in the number of probes around the electrodes. Ideally a 2D array of probes around the electrode could be used to map out the 2D potentials and flows due to the biasing. Downstream Langmuir and magnetic probes would be valuable to understand the parallel propagation of the potential and current (the magnetic sensors in NSTX were too far away from the electrode field lines to detect any perturbation in the present experiment).

On the theoretical side, the effects of intermittent SOL turbulence or 'blobs' should be incorporated into the modeling since the blob size is comparable to the electrode size (see figure 12(*a*)). For example, the $E \times B$ flow induced by the electrode might be limited by the blob diameter, and the blob transit time across the electrode flux tube may be comparable to the convective cell rotation time. Another possible effect is the finite ratio of ion gyroradius to electrode spacing ($\sim 0.2 \,\mathrm{cm}/1 \,\mathrm{cm}$), which could cause some ion orbit transport over this spacing.

Acknowledgments

References

[1] Lipschultz B *et al* 2007 *Nucl. Fusion* **47** 1189
[2] Loarte A 2007 *Nucl Fusion* **47** S203
[3] Staib P 1982 *J. Nucl. Mater.* **111/112** 109
[4] Fundamenksi W 2008 *Fusion Sci. Technol.* **53** 1023
[5] Cohen R H and Ryutov D D 1997 *Nucl. Fusion* **37** 621
[6] Ryutov D D *et al* 2001 *Plasma Phys. Control. Fusion* **43** 1399
[7] Cohen R H *et al* 2007 *Plasma Phys. Control. Fusion* **49** 1
[8] van Oost G *et al* 2003 *Plasma Phys. Control. Fusion* **54** 621
[9] Weynants R R *et al* 2005 *Fusion Sci. Technol.* **47** 202
[10] Strait E 1981 *Nucl. Fusion* **21** 943
[11] Decoste R *et al* 1994 *Phys. Plasmas* **1** 1497
[12] Schaffer M J *et al* 1996 *Nucl. Fusion* **36** 495
[13] Doerner R P *et al* 1994 *Nucl. Fusion* **34** 975
[14] Gravier E *et al* 2002 *Nucl. Fusion* **42** 653
[15] Motley R W and Glanz J 1982 *Phys. Fluids* **25** 2107
[16] LaBombard B 1990 *Nucl. Fusion* **30** 485
[17] Pitts R A and Stangeby P C 1990 *Plasma Phys. Control. Fusion* **32** 1237
[18] Winslow D L *et al* 1998 *Phys. Plasmas* **5** 752
[19] Thomsen H *et al* 2005 *Plasma Phys. Control. Fusion* **47** 1401

[20] Winslow D L and LaBombard B 2001 *J. Nucl. Mater.* **290–293** 788
[21] Rozhansky V A *et al* 1999 *Nucl. Fusion* **39** 613
[22] Carlson A 2001 *Phys. Plasmas* **8** 4732
[23] Hara J *et al* 1997 *J. Nucl. Mater.* **241–243** 338
[24] Counsell G *et al* 2003 *J. Nucl. Mater.* **313–316** 804
[25] Stockel J *et al* 2005 *Plasma Phys. Control. Fusion* **47** 635
[26] Roquemore A L *et al* 2008 *Rev. Sci. Instrum.* **79** 10F124
[27] Zweben S J *et al* 2009 *J. Nucl. Mater.* **390–391** 417
[28] Maqueda R J *et al* 2003 *Rev. Sci. Instrum.* **74** 2020
[29] Zweben S J *et al* 2004 *Nucl. Fusion* **44** 134